Tribological behaviour of microalloyed $Cu_{50}Zr_{50}$ alloy

A. Younes[a], S. De la Flor[b], S. J. Clark[c], J. Nutter[d], M. Birkett[a], J.O. Watson[e], M. Unthank[e], S. Gonzalez[a]

[a] Faculty of Engineering and Environment, Northumbria University, Newcastle upon Tyne, NE1 8ST, UK
[b] Department of Mechanical Engineering, ETSEQ, Universitat Rovira i Virgili, Av. Països Catalans 26,43007 Tarragona, Spain
[c]Department of Physics, Durham University, Science Labs, South Road, Durham DH1 3LE, UK
[d]Henry Royce Institute, Department of Materials Science and Engineering, University of Sheffield, Mappin Street, Sheffield, S1 3JD UK
[e]Faculty of Health and Life Sciences, Northumbria University, Newcastle upon Tyne NE1 8ST, UK

Abstract

Promoting the martensitic transformation through optimum microalloying with Fe and/or Mn was observed to be an effective method to enhance the wear resistance of the $Cu_{50}Zr_{50}$ at. % shape memory alloy (SMA). Among all the potential microelements and concentrations, partial replacement of Cu by up to 1 at. % Fe and Mn is of interest since from density functional based calculations large minimization of the stacking fault energy (SFE) of the B2 CuZr phase is predicted. For this reason, an effective martensitic transformation is expected. The largest decrease of the SFE from 0.36 J/m^2 to 0.26 J/m^2 is achieved with partial replacement of Cu by 0.5 at. % Fe. This results in the highest martensitic transformation upon wear testing, especially at highest load (15 N) for which the mass loss is 0.0123 g compared to 0.0177 g for $Cu_{50}Zr_{50}$ and a specific wear rate of 5.9 mm^3/Nm, compared to 8.5 for mm^3/Nm for $Cu_{50}Zr_{50}$. This agrees with the low coefficient of friction of 0.48±0.05 and low roughness of 0.200±0.013 µm of the Fe-containing alloy compared to that for $Cu_{50}Zr_{50}$, 0.55 and 0.415±0.026 µm, respectively. All the worn surfaces show the formation of abrasive grooves, being shallowest for the more wear resistant 0.5 at. % Fe alloy. The second more wear resistant alloy contains 0.5 at. % Mn. Wear mechanisms of abrasion, adhesion and delamination have been identified.

1. Introduction

Shape memory alloys (SMAs) have been extensively investigated over the years due to their interesting mechanical properties [1, 2]. After being deformed at room

temperature, SMAs can recover their original shape upon heating, the so-called Shape Memory Effect (SME). To achieve this, the external load has to be high enough to transform the metastable austenite phase into martensite [1]. Subsequently, the temperature has to be increased beyond A_f (the austenite finish temperature) to revert the martensite back into austenite [3]. A SMA of great interest is NiTi (nitinol) [4, 5], which displays pseudoelasticity, namely, the ability to recover elastically to its original zero strain shape [6]. The interest of NiTi stems from its good mechanical performance and high recovery ratio, however, the relative high cost of the element titanium, the low transformation temperature and high nickel content has limited its use. For this reason, there is a growing interest in replacing NiTi by more cost-effective SMAs. For this reason there has been intense effort in recent years to discover new SMAs [1], such as those corresponding to the Cu-Zr system, but the performance of these alloys is generally lower than that of NiTi [7]. An effective method to tune the performance of Cu-Zr SMAs is to promote the presence of microalloying elements in solid solution inside austenite by using rapid solidification and prevent their segregation to the grain boundaries [8]. This is of interest since the retention of elements in small concentrations inside the crystalline lattice of B2 CuZr austenite can alter its Stacking Fault Energy (SFE) [9]. For those elements that can decrease the SFE of austenite, the martensitic transformation of austenite is promoted [9]. For example, it was reported that for B2 CuZr austenite, partial replacement of 0.5 at. % Cu by some metallic elements could reduce the SFE and thus enhance the twinning propensity of austenite and promote the martensitic transformation [3, 8]. As a result, the wear resistance increases [10] and the ductility is also enhanced through a work-hardening process [11]. However, as was previously commented [12], the use of an increasing number of elements/microelements makes the performance prediction more difficult. For this reason, the use of models is helpful to screen a large number of potentially interesting micro alloying elements and subsequently select only those most promising for fabrication. In this regard, the aid of theory and simulations can be beneficial. In particular if bond breaking and making is involved in the process, then an accurate description of the energetics of the processes can be obtained from first principles electronic structure calculations. Here we have used density functional methods as implemented in the CASTEP electronic structure and materials properties package [13, 14]. It is possible to predict the effect of a microalloying element on lowering the SFE of B2 CuZr austenite and thus to predict the mechanical performance. In this

work, we have used first principles electronic structure methods for this purpose and done subsequent validation for the micro alloying elements Fe and Mn. Although it was previously reported that 0.5 at. % Fe promotes the martensitic transformation of B2 CuZr austenite [9], the effect of its concentration on the twinning propensity and wear behaviour have not been studied before. An element whose effect on B2 CuZr austenite has never been studied before is Mn, despite its potential interest due to its proximity to Fe in the periodic table. In fact, Mn has a well-known use in twinning induced plasticity steels [15].

Changes of the composition and cooling rate can in turn alter the alloy microstructure and therefore the mechanical performance of alloys [9, 11]. Higher cooling rate results in finer microstructures [16], which can be useful to prevent embrittlement of CuZr based SMAs since these alloys become brittle when the Cu grains are large [17, 8]. This effect is attributed to intergranular cracking mostly caused by high elastic anisotropy [18]. The effect of changes in composition is especially relevant for the CuZr system since its mechanical performance is very sensitive to even these small changes [19]. Wang et al. reported [19] that in order to obtain a 2 mm diameter casted CuZr alloy in an amorphous condition, the concentration of Zr should only vary between 34.5 to 37 at. %. This small window of 2.5 at. % illustrates how CuZr alloys are very sensitive to variations in composition and therefore a small change in composition can lead to a completely different microstructure. For example, for $Cu_{63}Zr_{37}$ at. % alloy, a mixture of amorphous and $Cu_{10}Zr_7$ crystalline phase is present while for $Cu_{65.5}Zr_{34.5}$ at. %, the crystalline phase formed is Cu_8Zr_3. Similarly, when the Zr content is in between the two (i.e. 35.5 at.%), no crystalline phase was formed [19]. Small changes in Cu concentration can also alter the crystallization process. For example, addition of ±2 at. % Cu can result in the formation of intermetallic phases such as $CuZr_2$ and $Cu_{10}Zr_7$ and can also alter the overall volume fraction of austenite and martensite of the alloy. Also, when the ratio of Cu to Zr is higher than 1:1 the alloy gets embrittled [20].

This clearly shows the importance of microalloying to tune the performance of CuZr SMAs. In this work, the effect of minor Fe and Mn additions on the wear performance of CuZr by using both experimental and computational techniques will be used.

2. Experimental procedure

The alloy ingots of nominal composition $Cu_{50}Zr_{50}$, $Cu_{49.5}Zr_{50}Fe_{0.5}$, $Cu_{49}Zr_{50}Fe_1$, $Cu_{49.5}Zr_{50}Mn_{0.5}$, $Cu_{49}Zr_{50}Mn_1$ and $Cu_{49}Zr_{50}Fe_{0.5}Mn_{0.5}$ alloys (at. %) coded in Table 1 were prepared from elements with purity higher than 99.9 at. %.

Table 1. Compositions coded for simplicity reasons.

Alloy	$Cu_{50}Zr_{50}$	$Cu_{49.5}Zr_{50}Fe_{0.5}$	$Cu_{49}Zr_{50}Fe_1$	$Cu_{49.5}Zr_{50}Mn_{0.5}$	$Cu_{49}Zr_{50}Mn_1$	$Cu_{49}Zr_{50}Fe_{0.5}Mn_{0.5}$
Code	-	$Fe_{0.5}$	Fe_1	$Mn_{0.5}$	Mn_1	$Fe_{0.5}Mn_{0.5}$

The master alloys were remelted (heated to a red heat) multiple times in a Ti-gettered high purity argon atmosphere to attain chemical homogeneity using a Compact Arc Melter MAM-1 Edmund Bühler. Rod samples of 2 mm diameter were obtained from the master alloy by copper mould casting in an inert gas atmosphere and a cooling system set at 20ºC. The structure of the as-cast samples was studied by SmartLab Rigaku XRD diffractometer with monochromated Cu Kα radiation (25° – 90° 2θ range). The Vickers hardness was measured on a WILSON VH1150 test instrument with an indentation load of 300 g and a holding time of 10 s. A differential scanning calorimeter (DSC) Mettler DSC-3+ was used to analyse the heat flow exchanges that take place during the transformation processes. Samples were placed in aluminium pans with a pierced lid in a nitrogen atmosphere with a gas flow of 50 mL/min. The Dynamic Mechanical Analysis (DMA) studies were performed in a temperature range of 30-420ºC/420-20°C with a heating and cooling rate of 10 °C/min. The ratio of the loss to the storage (tanδ) is often called damping and was measured as a function of temperature using a dynamic thermal mechanical analyser (TA Instruments DMA Q800) equipped with a liquid nitrogen cooling system. Measurements were conducted with a continuous heating rate of 5 °C/min in the 30-100ºC temperature range and with a frequency of 0.2 Hz. Samples of 2 mm in diameter were subjected to flexural loading in the 3-point bending configuration (with a low-friction, self-adjusting 3-point bending clamp) at a strain amplitude of 0.03%. The microstructure was revealed using Kroll's reagent (2 ml HF, 6 ml HNO_3, and 92 ml H_2O) before being investigated by scanning and transmission electron microscopy (SEM and TEM, respectively). Dry sliding wear experiments were conducted using a pin-on disc (DUCOM Micro POD) in air at room temperature following the ASTM-G99 standard. The pins were made by cutting the as-cast rods transversely and the resulting cross-sections were ground to have a flat surface by using 4000 grit paper. Subsequently, the flat surfaces of the pins were wear

tested ~~using the as-casted rods and their surfaces were the mirror surface polished using 4000 grit paper prior to wear testing~~ against a flat counterbody disc of 60 HRC hardened SS304 stainless steel of 0.6 mm (R_a) surface roughness provided by the company DUCOM. Tests were performed at increasing loads of 1, 5, 10 and 15 N at a sliding velocity of 0.5 m/s for a sliding distance of 1800 m (i.e., for 1 hour). The mass loss is the average of at least 3 samples and was obtained by measuring the weight of the pins before and after wear tests using an analytical balance (Fisherbrand™ Analytical Balance, ±0.1 mg). The average roughness and profile were analyzed using an Alicona InfiniteFocus 3D profilometer and the profiles were obtained by averaging 5 measurements.

The computational modelling used density functional methods implemented in CASTEP where a plane-wave basis set is used to describe the electronic states. Accurate pseudopotentials [21] describe the valence electron interactions with ionic cores and the generalised gradient formalism [22] for the electronic exchange-correlation interactions. The basis set (plane-wave kinetic energy cut-off and k-point Brillouin zone sampling) are converged to 1meV/cell, with geometry optimisations considered converged when atomic forces are less than 0.01eV/A.

3. Results and discussion

In order to assess the effect of the concentration of Fe and Mn on the wear performance, the CuZr-based alloys were characterized before and after the wear tests. This enables analysis of microstructural changes and plastic deformation by XRD.

3.1. Modelling for Stacking Fault Energy predictions

The lowest energy slip plane of CuZr in the B2 structure is in the [011] plane sliding in the {100} direction (and given the system is cubic, [101]{010} and [110]{001} are also equivalent slip systems). A schematic of this is shown in Fig. 1. A supercell is constructed containing 40 monolayers of CuZr normal to [011] and half of the atoms slipped in steps of 1/10 of the lattice parameter, forming 2 slip planes (forced by the periodicity of the system). This supercell was determined by converging total energies as a function of supercell size until the stacking fault energy was converged to better than 0.002 J/m^2. The total energy of the system is calculated as the plane slides a distance of a whole unit cell. We have performed calculations of the system with

“defect” atoms on the slip plane replacing a Cu atom with a range of various other species, to search for lower SFEs and also at two concentrations. Fig. 2 (a) shows the slip plane energies for the [001], [011] and [111] planes in various orthogonal slip directions, confirming that [011]{001} is the lowest energy, while in (b) the relative total energies are shown for the parent alloy (i.e., base) containing no substitutional atoms and also for Fe and Mn substitutions as well as the co-microalloy with a mixed substitution of Fe/Mn. All Fe and Mn alloys cause a significant decrease of the SFE, however, we do not observe the huge energy reductions shown in [9], including a 3-fold decrease in stacking fault energy with Fe substitution. The $Fe_{0.5}$ plot does not lie between Fe_1 and Fe_0 because partial replacement of Cu in B2 CuZr by 0.5 at. % Fe decreases the stacking fault energy (SFE) of Fe_0 (base) the largest (i.e., minimum energy (J/m^2)). However, partial replacement by 1 at. % Fe (Fe_1) is not so effective decreasing the SFE of the base Fe_0 alloy, for this reason their values are relatively close to each other. The addition of Fe as microalloying element replacing Cu in B2 CuZr was reported by Wu et al. [9] to reduce the SFE. However, they solely studied the effect for a concentration in microalloying element in solid solution of 0.5 at. %. In this study we have expanded this by investigating the effect of microalloying with 1 at. % Fe and also the effect of the novel element Mn on the tribological performance of B2 CuZr using pin-on-disc experiments.

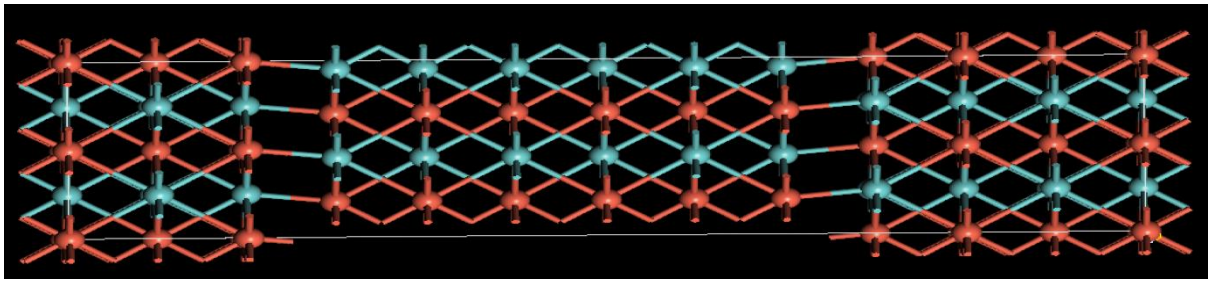

Fig. 1. Model of B2 CuZr showing the position of the atomic structure, Cu (brown) and Zr (blue) in the [011] plane and {100} direction.

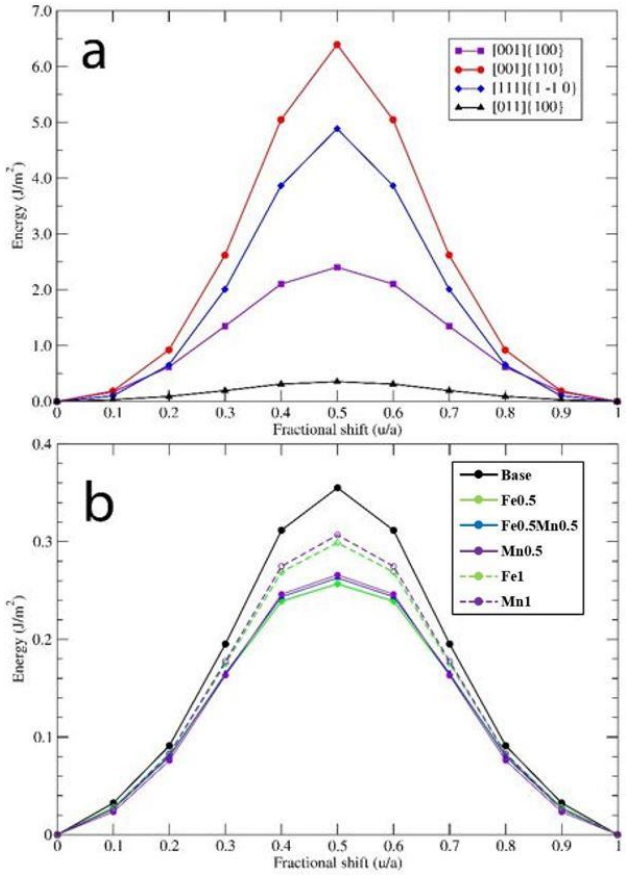

Fig. 2. (a) Various stacking fault energies of slip planes in the B2 phase of CuZr. (b) Stacking fault energy on the lowest energy [011]{100} slip system of the B2 CuZr phase with half Cu on the slip plane substituted by Fe and Mn (solid line) and similarly for a doubled concentration (dashed).

3.2. Structural characterization of as-cast alloys

The experimental results of Fig. 3 show the backscattered SEM images of as-cast $Cu_{50}Zr_{50}$ (Fig. 3a), $Cu_{49}Zr_{50}Fe_1$ (Fig. 3c) and $Cu_{49}Zr_{50}Mn_1$ (Fig. 3e) alloys and the corresponding EDX scans from the dendrites (see arrows) (Fig. 3b, 3d and 3f). The microstructural differences among the three compositions are relatively small, as could be expected considering their similar composition. For all of them, the microstructure basically consists of dendrites from 2 μm to 10 μm in length, embedded in a fine crystalline matrix. To understand the nature of the as-cast samples, compositional EDX analysis and crystallographic analysis by XRD have been performed. Considering that for a microalloying element to have an effect on the twinning propensity of austenite it should be present in solid solution inside the crystalline lattice [9], their presence has been investigated by SEM-EDX. This analysis has been carried out from the dendrites located at approximately the centre of the samples, where the

cooling rate is the lowest and thus the elements are more prone to segregation (i.e., if there is no segregation in the centre, then it will not occur close to the border where the cooling rate is faster).

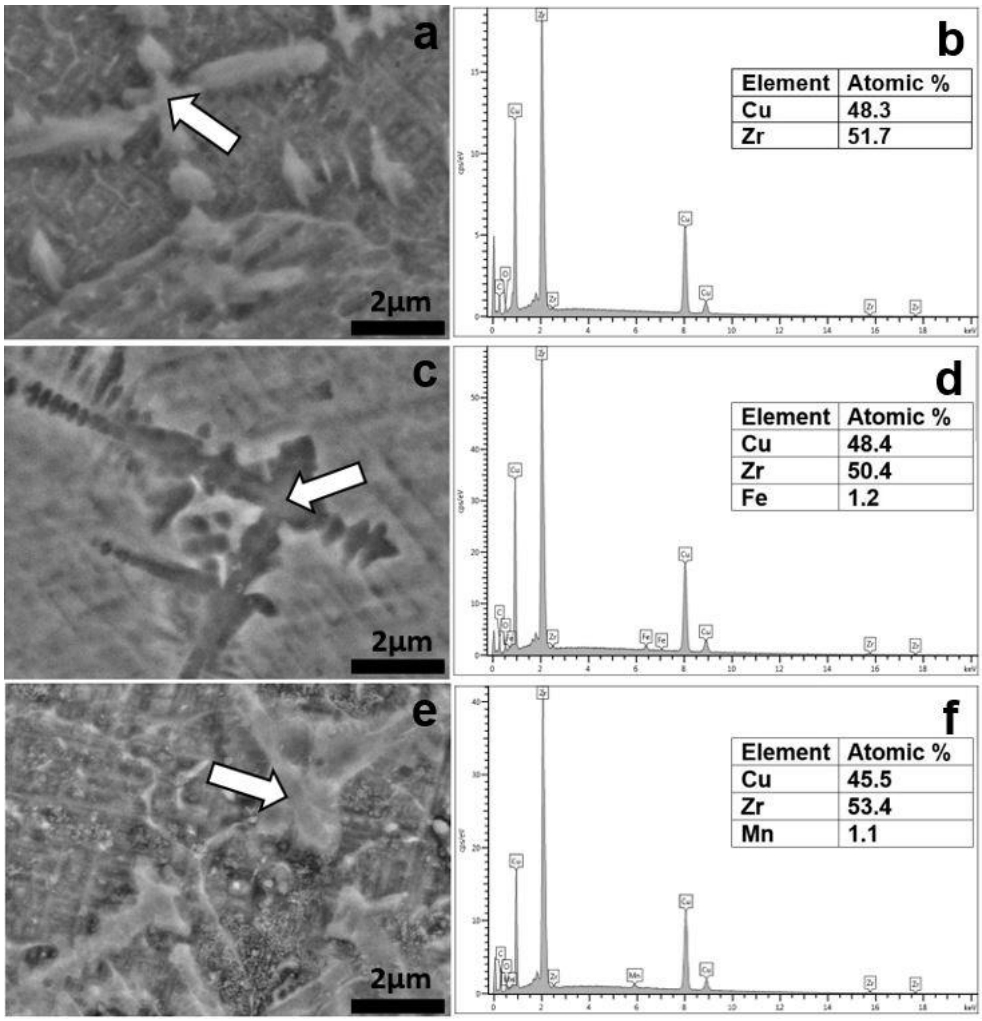

Fig. 3. Backscattered SEM images of as-cast (a) $Cu_{50}Zr_{50,}$ (c) $Cu_{49}Zr_{50}Fe_1$ (e) $Cu_{49}Zr_{50}Mn_1$ alloys and corresponding EDX scans of the dendrites indicated with an arrow (b), (d) and (f), respectively.

To get an average composition value of the dendrites, EDX analysis was carried out on more than 3 dendrites per composition and the ones shown in Fig. 3 are the most representative ones. For $Cu_{50}Zr_{50}$ (Fig. 3a), EDX analysis shown in Fig. 3b indicates that the composition is 48.3 at.% Cu and 51.7 at. % Zr. For $Cu_{49}Zr_{50}Fe_1$ (Fig. 3c) the composition is 48.39 at.% Cu, 50.42 at.% Zr and 1.19 at.% Fe (Fig. 3d). Similar results have been obtained for the $Cu_{49}Zr_{50}Mn_1$ at. % alloy (Fig. 3e) for which the composition of the dendrites is 45.47 at.% Cu, 53.43 at.% Zr and 1.10 at.% Mn (Fig. 3f). All results are listed in Table 2. The results show that concentration of microalloying element in the crystalline phase is close to the nominal composition, 1 at. % Fe and 1 at. % Mn

respectively and thus confirms the presence of microalloying elements in solid solution inside the crystalline phase.

Table 2: Composition in at. % of the dendrites indicated with arrows (Fig. 3).

Composition (at. %)	Cu	Zr	Fe	Mn
Fig. 3a ($Cu_{50}Zr_{50}$) dendrite	48.30	51.70	-	-
Fig. 3c ($Cu_{49}Zr_{50}Fe_1$) dendrite	48.39	50.42	1.19	-
Fig. 3e ($Cu_{49}Zr_{50}Mn_1$) dendrite	45.47	53.43	-	1.10

3.3. Thermal and thermomechanical behaviour

In order to understand the thermal and thermomechanical behaviour of the as-cast $Cu_{50}Zr_{50}$, $Cu_{49.5}Zr_{50}Fe_{0.5}$, $Cu_{49}Zr_{50}Fe_1$, $Cu_{49.5}Zr_{50}Mn_{0.5}$, $Cu_{49}Zr_{50}Mn_1$ and $Cu_{49}Zr_{50}Fe_{0.5}Mn_{0.5}$ alloys, they have been studied upon heating (Figs. 4A) and upon cooling (Figs. 4B) by DSC and DMA (Fig. 4C). The transformation temperatures have been summarized in Table 3, which shows A_s, A_f and martensite start (M_s) temperatures obtained from DSC (Fig. 4A and 4B), as well as the austenite peak (A_p) obtained from DMA (Fig. 4C). For the parent $Cu_{50}Zr_{50}$ alloy and the Fe-containing alloys, a relatively large endothermic peak is observed associated to the transformation of martensite into austenite, where A_s and A_f are austenite start temperature and austenite finish temperature, respectively.

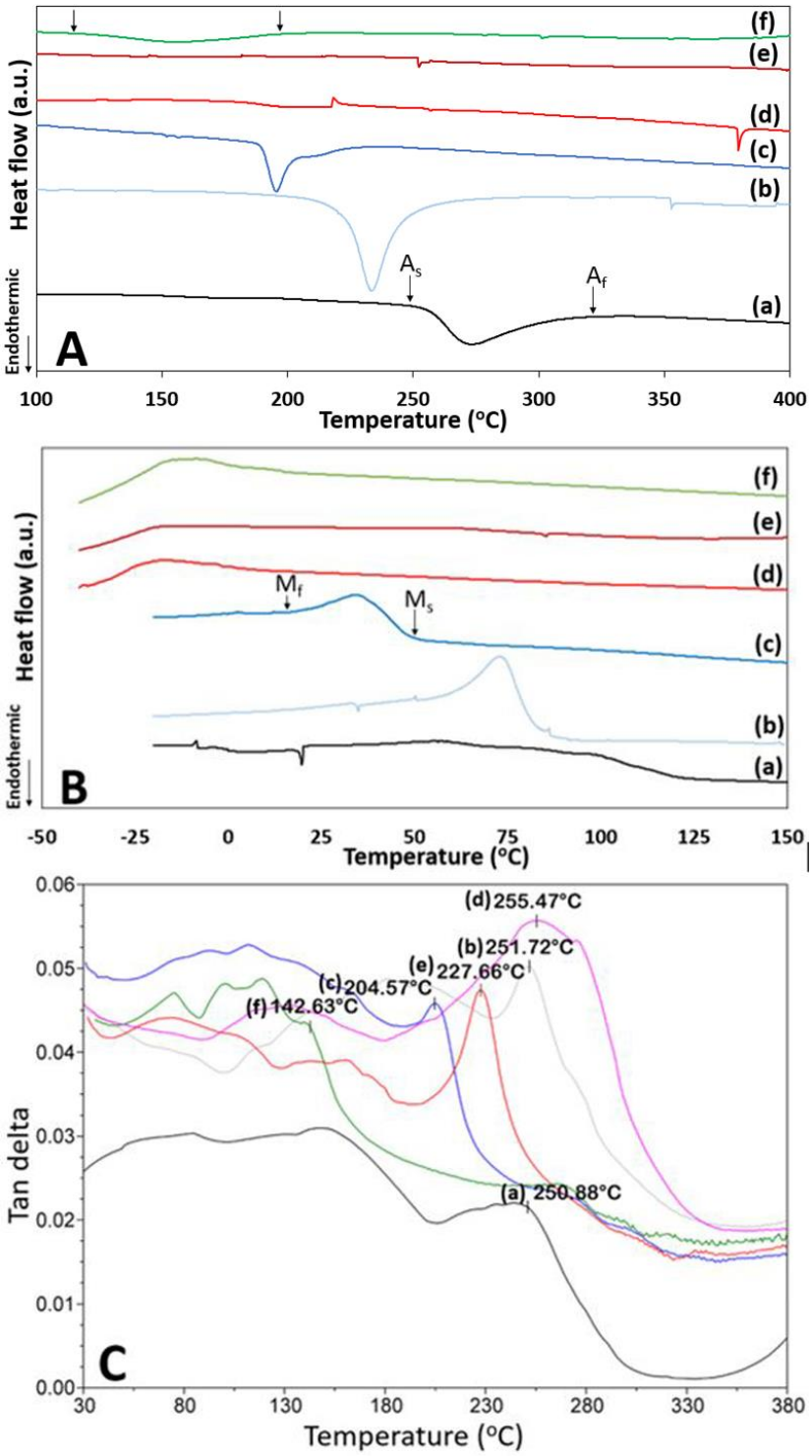

Fig. 4. DSC scans upon (A) heating and (B) cooling and (C) DMA scans upon heating for (a) $Cu_{50}Zr_{50}$, (b) $Cu_{49.5}Zr_{50}Fe_{0.5}$, (c) $Cu_{49}Zr_{50}Fe_1$, (d) $Cu_{49.5}Zr_{50}Mn0.5$, (e) $Cu_{49}Zr_{50}Mn_1$ and (f) $Cu_{49}Zr_{50}Fe_{0.5}Mn_{0.5}$.

For $Cu_{50}Zr_{50}$, the austenite phase starts the transformation (A_s) at around 250°C and it is completed (A_f) at around 323°C. For $Cu_{49.5}Zr_{50}Fe_{0.5}$ the transformation temperatures are A_s = 205°C and A_f = 273°C while for $Cu_{49}Zr_{50}Fe_1$ they are A_s = 188°C and A_f = 222°C. These results clearly show that increasing addition of Fe progressively

shifts the transformation temperatures to lower values. However, for the Mn-containing alloys, i.e. $Cu_{49.5}Zr_{50}Mn_{0.5}$ and $Cu_{49}Zr_{50}Mn_1$, the austenitic transformation peak is not detected. For $Cu_{49}Zr_{50}Mn_{0.5}Fe_{0.5}$ the intensity of the peak is very small and broad, with A_s = 115ºC and A_f =197ºC, and this is consistent with intermediate behaviour between that of the alloys with only Fe (showing peak) or with only Mn (no peak). This would not be possible to explain in terms of differences in volume fraction of martensite and austenite present upon rapid cooling for the different compositions since the XRD scans show that their relative intensity is similar (see section 3.5). To further investigate this, DMA measurements have been conducted and plotted as tan delta versus temperature (Fig. 4C). The presence of transformation peaks not only for Fe-containing alloys but also for those containing Mn, proves that DMA is able to detect transformations that could not be detected by DSC, since DMA measures the thermomechanical response rather than only the thermal behaviour of the alloys [23, 24]. The detection of more irregular curves consisting of small peaks from about 50 to 200 °C are attributed to the elimination of internal defects for the alloys containing Mn when compared to those containing Fe. This is in agreement with previous observations for which the amount of lattice defects present in SMAs can affect the 'intensity' of the observed peaks in DSC analysis. The DMA curves of Fig. 4C show a high intensity peak attributed to the transformation of martensite into austenite. Moreover, the transformation peaks shift to lower temperatures with increasing concentration of Fe, which is in agreement with the DSC curves and the shift is similar for the Mn-containing alloys.

Table 3. Transformation temperatures A_s, A_f and Ms from DSC scans, A_p from DMA scans for all alloys.

Composition (at.%)	A_s (ºC)	A_f (ºC)	M_s (ºC)	A_p (ºC)
$Cu_{50}Zr_{50}$	250	323	124	251
$Cu_{49.5}Zr_{50}Fe_{0.5}$	205	273	91	252
$Cu_{49}Zr_{50}Fe_1$	188	222	54	205
$Cu_{49.5}Zr_{50}Mn_{0.5}$	-	-	-	255
$Cu_{49}Zr_{50}Mn_1$	-	-	-	228
$Cu_{49}Zr_{50}Fe_{0.5}Mn_{0.5}$	115	197	4	143

3.4. Wear tests

To study the effect of the microalloying elements Fe and Mn on the mechanical performance of B2 austenite, wear tests have been performed. Fig. 5 shows the evolution of the mass loss (g)(Fig. 5a) and specific wear rate (mm^3/Nm) (Fig. 5b) for all the samples tested for 1h at room temperature (RT) at loads of 5, 10 and 15 N.

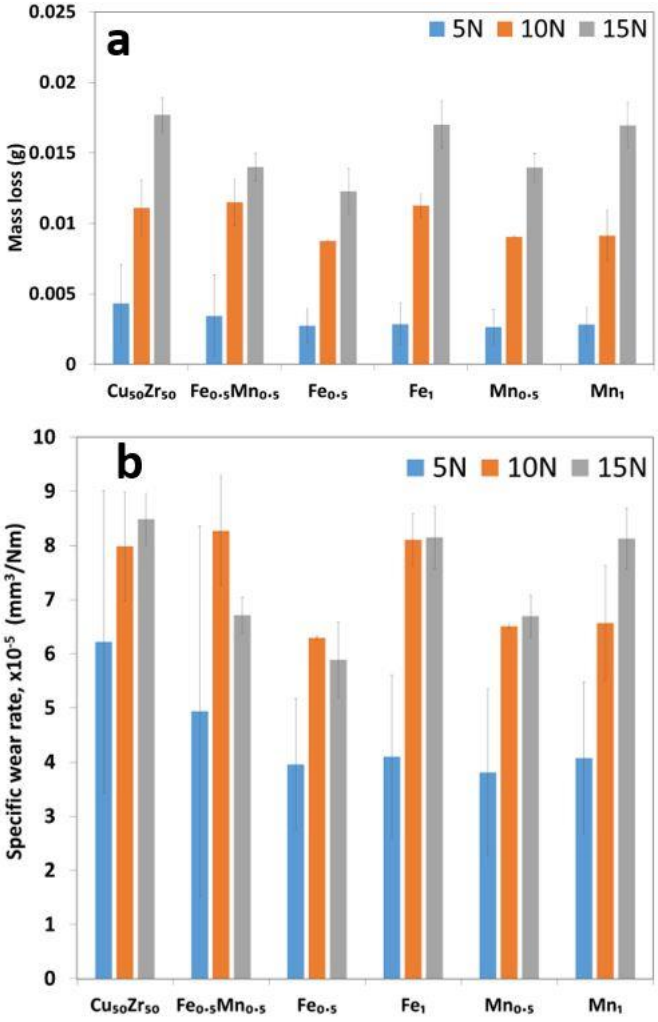

Fig. 5. (a) Evolution of mass loss and (b) evolution of specific wear rate for the different alloys (code in parenthesis): $Cu_{50}Zr_{50}$, $Cu_{49}Zr_{50}Fe_{0.5}Mn_{0.5}$ ($Fe_{0.5}Mn_{0.5}$), $Cu_{49.5}Zr_{50}Fe_{0.5}$ ($Fe_{0.5}$), $Cu_{49}Zr_{50}Fe_1$ (Fe_1), $Cu_{49.5}Zr_{50}Mn_{0.5}$ ($Mn_{0.5}$) and $Cu_{49}Zr_{50}Mn_1$ (Mn_1) and loads up to 15 N applied for 1 h.

For all the compositions, the mass loss (Fig. 5a) increases with load increase, ~~but this increase is not linearly proportional with the load and it depends on the composition.~~ ~~the~~ For the $Cu_{50}Zr_{50}$ alloy, the mass loss for a 5N load is 0.00255 g, increasing to 0.0111g and 0.0177g for 10 N and 15 N, respectively. However, the trend is different when Cu is replaced by Fe or Mn. Among all the compositions, the lowest mass loss

values at 10 N (0.00875 g) and 15 N (0.0123 g) are observed when Cu is partly replaced by 0.5 at. % Fe. However, for 5 N load, the mass loss is similar (i.e., within the error range) for all the compositions tested. This suggests that for 15 N load, the alloy that exhibits the most effective work-hardening upon twinning is the one containing 0.5 at. % Fe. This is consistent with the fact that for this composition the stacking fault energy is the smallest (0.26 J/m^2, see Fig. 2) and therefore stress-induced twinning is promoted the most [3, 8]. Fig. 5b shows the specific wear rate in (mm^3/Nm) which can be calculated from the following equation:

$$W = V/L\ F \qquad (1)$$

where W corresponds to specific wear rates (mm^3/Nm), V is the wear volume (mm^3), L is the sliding distance (m) and F is the applied load (N). The sliding distance and applied load (i.e., 5, 10 and 15 N) for all the tested samples is the same. Therefore, the only difference in wear rate is due to the differences in wear volume. From Fig. 5b it is observed that $Fe_{0.5}$ has the lowest wear volume and therefore lowest specific wear rate, around 5.9 mm^3/Nm, compared to 8.5 for mm^3/Nm for $Cu_{50}Zr_{50}$ at 15 N load, which agrees with the lowest mass loss value (Fig. 5a). That can be attributed to the accelerated martensitic transformation and work-hardening, which is highest for the alloy containing 0.5 at. % Fe. Despite all pins have a flat surface before testing to ensure maximum contact between pin and disc, a complete surface contact between the two bodies (pin and disc) throughout the test (1h) can only be guaranteed when testing at 10 and 15 N. This explains the high uncertainty values for 5N compared to 10 and 15N. Moreover, only for 10 and 15 N load the stress is high enough to transform austenite into martensite.

~~For sake of simplicity in Fig. 5b, only 10 and 15N loads were presented as they are high enough to transform austenite into martensite. In addition, higher loads (i.e. 10 and 15N) ensure constant pin-disc contact throughout the testing period of 1h.~~

There is a general inverse correlation between the total wear debris produced ~~(i.e., mass loss)~~ and the alloy hardness through Archard's equation [25]. For this reason, higher hardness involves higher wear resistance. The hardness of the as cast $Cu_{50}Zr_{50}$ alloy is 2.82±0.43 GPa and does not exhibit significant change after testing at 15N. However, the hardness of the as cast $Cu_{49.5}Zr_{50}Fe_{0.5}$ alloy increases from 3.39±0.36 GPa to 3.65±0.2 GPa after testing at 15 N load. These values are similar to those previously reported [26]. The work-hardening effect upon loading with 15 N is attributed to partial transformation from austenite into martensite, a harder phase, as can be deduced from the change in relative intensity of the XRD peaks ~~of~~ ~~Fig. 10~~ and the TEM images in section 3.5. ~~of Fig. 11~~. ~~These results will be discussed in more detail in section 3.5.~~

~~For 10 and 5 N load, the amount of austenite that can transform into martensite decreases when the load decreases (Fig. 5) and therefore as the load decreases, the mass loss becomes more similar for all the compositions.~~ However, the appropriate concentration of microalloying element is also an important factor when tailoring the SFE. In fact, for Fe_1 addition, the mass loss values for 10 N (0.011 g) and 15 N (0.017 g) are higher than for $Fe_{0.5}$. The higher mass loss indicates that the alloy does not work-harden so effectively as the one with $Fe_{0.5}$ due to the fact that the SFE for Fe_1 (0.3 J/m^2) is higher than for $Fe_{0.5}$ (0.26 J/m^2) as shown in Fig. 2.

The effect of Mn addition on the wear resistance is similar but not so remarkable as that of Fe as shown in Fig. 5a and 5b. The addition of $Mn_{0.5}$ as a microalloying element also enhances the wear performance as the mass loss increases to only 0.014 g at 15N compared to 0.017g for $Cu_{50}Zr_{50}$. This suggests that Mn also promotes stress-induced martensitic transformation during the wear test, but less efficiently than $Fe_{0.5}$. The slightly higher SFE (Fig. 2) for $Mn_{0.5}$ (0.27 J/m^2) than for $Fe_{0.5}$ (0.26 J/m^2) confirms these results.

For the Mn_1 alloy, the mass loss values for 15 N are very similar and within the error range of the $Cu_{50}Zr_{50}$ and Fe_1 alloys. This is in accordance with the similar SFE for Mn_1 (0.31 J/m^2) and Fe_1 (0.3 J/m^2) but smaller than that of $Cu_{50}Zr_{50}$ (0.36 J/m^2). This slight mismatch is attributed to the relatively large experimental error values of mass loss at 15 N load. For the $Fe_{0.5}Mn_{0.5}$ co-microalloyed alloy, the mass loss values at 15 N are intermediate between that of $Fe_{0.5}$ and $Mn_{0.5}$ and agree with the intermediate SFE values (Fig. 2), between 0.27 J/m^2 for $Mn_{0.5}$, and 0.26 J/m^2 for $Fe_{0.5}$. These results confirm the good agreement between our experiments and the model. The results also indicate that when testing at 15 N, the wear resistance is maximum when Cu is partly replaced by 0.5 at. % Fe, followed by 0.5 at. % Mn, thus resulting in a lifetime enhancement of the parent alloy of about 30.5 % and 21 %, respectively.

Analysis of wear tracks and wear debris on the pin and the SS304 counterbody was investigated using SEM and EDX. Fig. 6 shows SEM images and EDX scans from the worn surface of the $Cu_{49.5}Zr_{50}Fe_{0.5}$ pin tested at 15 N load. This composition is of interest since it exhibits the highest wear resistance among all the studied the alloys (Fig. 5). The general image Fig. 6a shows the presence of long continuous grooves caused by ploughing, which is a common mechanism of abrasive wear [27, 28]. From the pin surface, different features can be observed. Among them, wear scars, which are signs of delamination generated by shear forces acting on the pin upon sliding.

When testing at 15 N load, the surface of the pin deforms plastically and subsurface cracks nucleate and propagate leading to formation of sheet-like wear features (see circle on Fig. 6b) [29]. This wear mechanism is responsible for the plastic deformation thus resulting in partial transformation from austenite into martensite. This can be proven from the increase in intensity of the XRD peaks associated to martensite and decrease of those associated to austenite after wear tests as shown in section 3.5. ~~(Fig. 10b)~~. In addition, two distinctive features can be seen, small debris particles distributed across the surface (Fig. 6c) and smeared patches (Fig. 6d) along the wear direction. EDX microanalysis of the small particles of dark tonality indicate that these particles are rich in oxygen (33.2 at.% O, 1.6 at.% Fe, 0.36 at.% Cr, 40.6 at.% Cu, 24.4 at.% Zr) and have slightly higher concentration in Cu than Zr. These particles therefore they may correspond to $Cu_{10}Zr_7$ oxides. This is consistent with the detection of XRD peaks associated to $Cu_{10}Zr_7$ (see Fig. 11~~0~~). These dragged hard third body particles plough through the surface and form grooves (Fig. 6a). In addition, the surface of the worn pin exhibits long smeared patches of up to 250 μm, which are oriented along the direction of grooves. EDX microanalysis indicate that these patches have a composition of 17.8 at.% O, 13.3 at.% Cr, 44.6 at.% Fe, 4.9 at.% Ni, 9.9 at.% Cu and 9.6 at.% Zr. The high percentage of Fe and presence of Ni and Cr indicates that these smeared patches are coming from the counterbody (SS304) as transferred material. This transference can be described by the mechanism of adhesive wear [30]. These results have been compared to the reference material, the $Cu_{50}Zr_{50}$ pin tested at the same conditions (15 N load) as shown in the SEM images and EDX scans of Fig. 7. This composition is of interest since it exhibits the lowest wear resistance among all the studied alloys (Fig. 5). The general image Fig. 7a shows the presence of long continuous grooves indicative of abrasive wear, which are similar to those observed for $Fe_{0.5}$ at. % but they are more distinct and abundant for $Cu_{50}Zr_{50}$. Furthermore, longer and more abundant continuous subsurface cracks that propagate towards the surface are seen in $Cu_{50}Zr_{50}$ (Fig. 7b). These subsurface cracks are associated to delamination wear and their morphology is consistent with observations from different authors including Li et al. [31]. In order to identify the nature of the small particles of dark tonality shown in Fig. 7c, EDX microanalysis has been conducted. The results (46.9 at.% O, 1.2 at.% Fe, 0.09 at.% Cr, 25.3 at.% Cu, 26.6 at.% Zr) indicate that these particles are rich in oxygen and have similar concentration in Cu and Zr. These oxide particles are similar in terms of shape, size and concentration in

O to those reported for Fe0.5 at. % in Fig. 6c. Additionally, Fig. 7d shows the surface of the worn pin exhibiting long smeared patches of around 150 μm length oriented along the direction of the grooves. EDX microanalysis indicate that these patches have a composition of 19.3 at.% O, 13.8 at.% Cr, 37.5 at.% Fe, 3.9 at.% Ni, 13.8 at.% Cu and 14.7 at.% Zr. The high percentage of Fe and presence of Ni and Cr indicates that these smeared patches are coming from the counterbody (SS304) as transferred material which is a common feature of adhesive wear. Both, the composition and morphology of the oxide particles and smeared patches are similar to those detected for the $Fe_{0.5}$ at. % alloy (Fig. 6) while the main difference is the presence of more profuse and well-defined grooves for the $Cu_{50}Zr_{50}$ pin. This has been studied in more detail in Fig. 10.

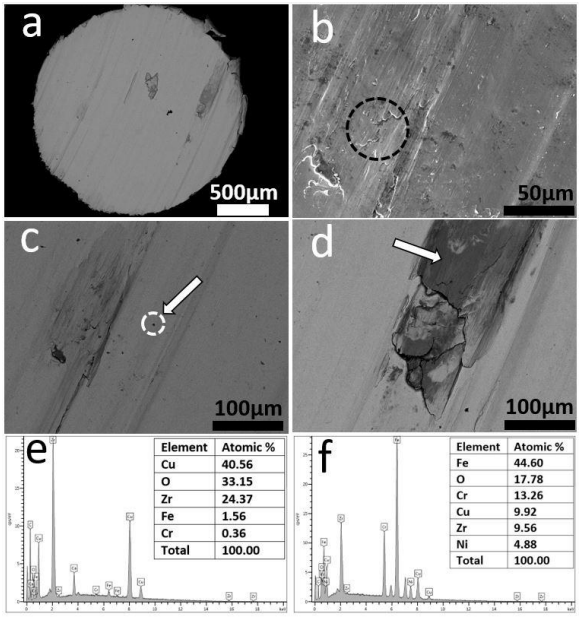

Fig. 6. SEM images from the 2 mm diameter $Cu_{49.5}Zr_{50}Fe_{0.5}$ pin tested at 15N load. (a) General and detailed images showing (b) wear scars (circle) (c) dark particles (arrow) and (d) patches (arrow) and corresponding EDX scans, respectively.

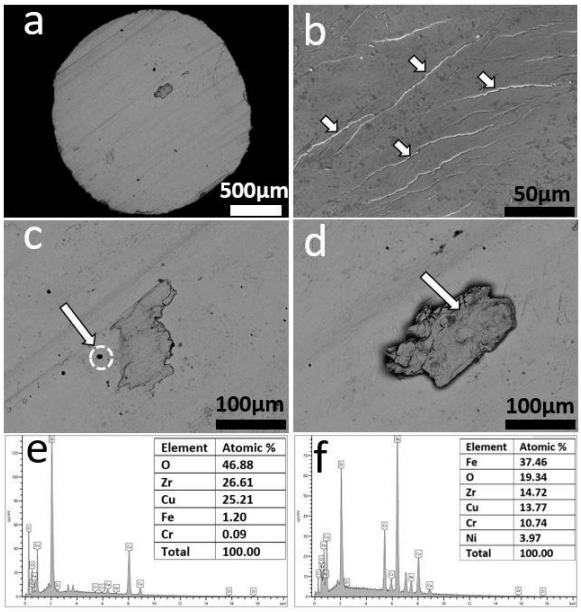

Fig. 7. SEM images from the 2 mm diameter $Cu_{50}Zr_{50}$ pin tested at 15N load. (a) General and detailed images showing (b) wear scars (small arrows) (c) dark particles (arrow) and (d) patches (arrow) and corresponding EDX scans, respectively.

In sliding wear, the performance of the entire tribosystem counts. For this reason, the surface of the SS304 counterbody (Fig. 8) after the wear tests for the $Fe_{0.5}$ (Fig. 8a and b) and $Cu_{50}Zr_{50}$ pin (Fig. 8c and d) at 15 N load have been also studied. The

backscattered SEM image of Fig. 8a shows some patches (i.e., attached wear debris) of clear tonality heterogeneously attached to the wear track of the SS304 counterbody.

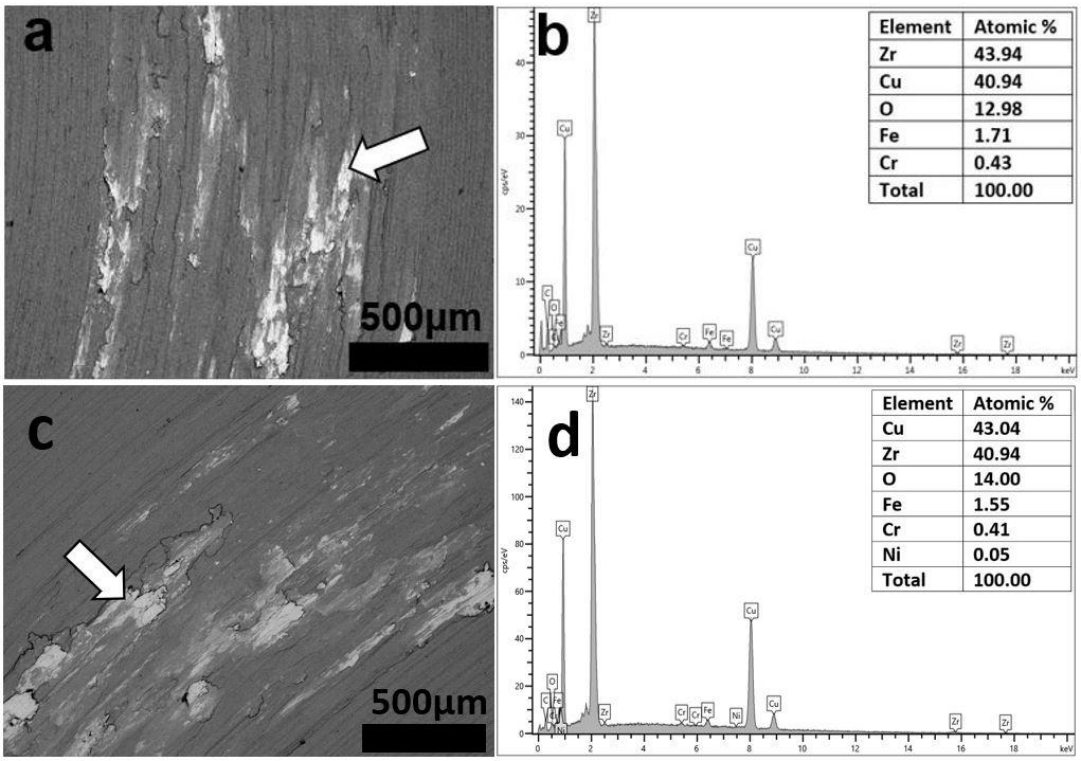

Fig. ~~7~~8. a) SEM backscattered images of SS304 counterbody worn surfaces after wear testing at 15 N (a) the $Fe_{0.5}$ and (c) the $Cu_{50}Zr_{50}$ pins and corresponding b) and d) SEM-EDX scans from the transferred material (see arrow), respectively.

The bright colour of the patches indicates the presence of heavier elements than those of the SS304 disc (grey background) and therefore they might be associated to material detached from the pin. This process of metal removal occurs by adhesion of the material from the pin surface onto the SS304 counterbody [30]. This can be proven from EDX (Fig. 8b) as the content of Cu and Zr at.% roughly makes up 84% of the highlighted wear track (13 at.% O, 0.4 at.% Cr, 1.7 at.% Fe, 40.9 at.% Cu, 43.9 at.% Zr). For the $Cu_{50}Zr_{50}$ sample (Fig. 8c) the amount of material attached onto the SS304 counterbody is more abundant and of larger size, up to about 400 µm compared to about 200 µm for the $Fe_{0.5}$ alloy. This is consistent with the higher mass loss and wear rate (Fig. 5) and the more abundant grooves (Fig. 6 and 7) for $Cu_{50}Zr_{50}$ compared to the $Fe_{0.5}$ alloy. The morphology of these patches is similar to those observed by other authors [32] but they are not so elongated for our materials probably because the presence of brittle intermetallic phases makes the patches more hard and brittle and therefore more difficult to spread. EDX analysis of these patches (see arrow in Fig. 8d) indicate that the chemical composition is 14 at.% O, 0.4 at.% Cr, 1.55 at.% Fe, 43

at.% Cu and 40.9 at.% Zr, very similar to those for Fe0.5 but slightly poorer in Fe as could be expected considering that the $Cu_{50}Zr_{50}$ alloy does not contain Fe.

Another important parameter to investigate the wear behaviour [33] is the coefficient of friction, i.e., the resistance encountered when moving one object over another. A small friction coefficient indicates high wear resistance [34]. The coefficient of friction generally exhibits two stages during the duration of the wear test, the first stage is a short period at the start of the test with a rapid increase of coefficient of friction followed by stabilization of the coefficient of friction throughout the rest of the test, also called the steady-state stage [33, 35]. Fig. 9 shows the coefficient of friction (COF) as a function of the testing time from 0 to 3,600 seconds. The average values of the COF are 0.48±0.05, 0.49±0.04, 0.51±0.04, 0.54±0.03, 0.55±0.04 and 0.59±0.04 for the $Fe_{0.5}$, $Fe_{0.5}Mn_{0.5}$, $Mn_{0.5}$, Fe_1, $Cu_{50}Zr_{50}$ and Mn_1 alloys, respectively. The lowest value for the $Fe_{0.5}$ alloy is consistent with the lowest mass loss and specific wear rate (Fig. 5) and therefore this alloy exhibits the highest wear resistance. These values are not far from those reported in the literature, from about 0.4 to 0.6 for $Cu_{60}Zr_{30}Ti_{10}$ at. % [36] and about 0.35 to 0.45 for a Cu-BMG (bulk metallic glass) of similar composition to the alloys of this work, when sliding against EN26 steel [27].

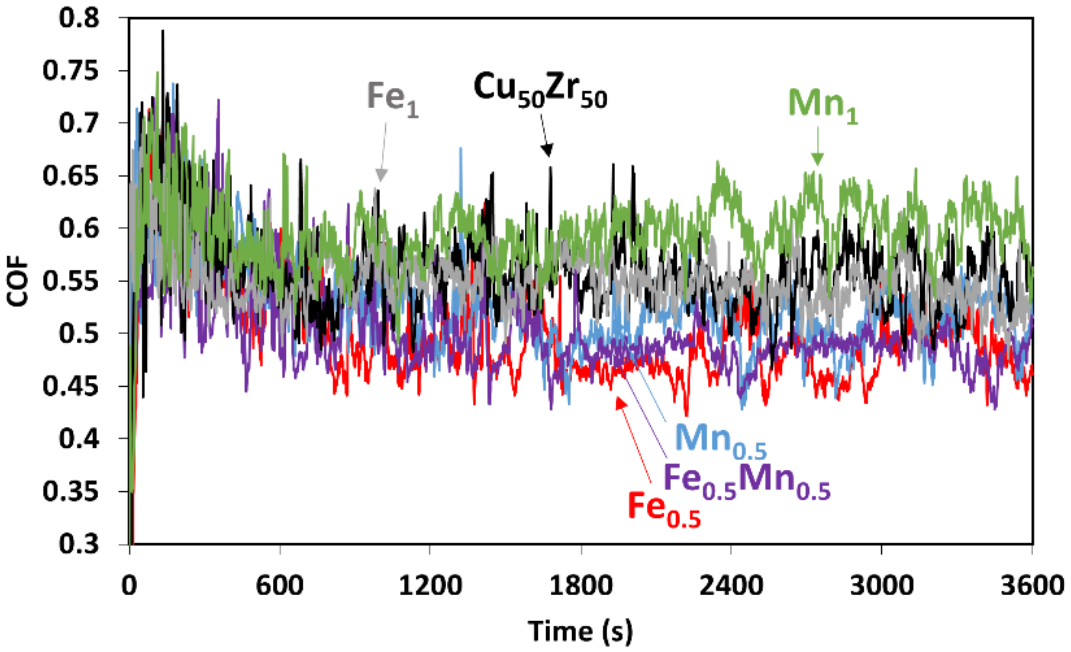

Fig. 89. The coefficient of friction as a function of the testing time.

To analyse the differences in wear behaviour of all the compositions in more detail, the worn surfaces of the samples tested at 15 N load have been observed under the

profilometer. This loading condition has been selected since maximum differences in mass loss among all the compositions are obtained for 15 N load (Fig. 5) and therefore, maximum differences of the worn surfaces are expected. In order to quantify the roughness of all the alloys wear tested at 15 N load for 1 hour, representative surfaces of each worn pin surface (square of 360mm^2 size) were analyzed using a profilometer (Fig. 10). Parallel grooves on the worn surface of all samples after sliding are observed. It was found that the average roughness values measured perpendicular to the grinding direction (R_a) for $Cu_{50}Zr_{50}$, Fe_1 and Mn_1 were 0.415±0.026, 0.375±0.004 and 0.356±0.021 µm, respectively. These values of R_a were higher than those for $Mn_{0.5}$ and $Fe_{0.5}Mn_{0.5}$, 0.301±0.003 and 0.247±0.010 µm, respectively. These results are in agreement with the values of mass loss (Fig. 5) and COF (Fig. 9). The worn surface of the $Fe_{0.5}$ alloy tested at 15 N exhibits a minimum roughness of 0.200±0.013 µm and the COF is the lowest.

The compositions with higher roughness exhibit deeper grooves because more material is ploughed out from the surface while the sample with lowest roughness ($Fe_{0.5}$) exhibits the shallowest grooves. This type of wear is called abrasive wear since ploughing results in the removal of a certain volume of material thus resulting in the formation of abrasive grooves on the weaker surface of two surfaces in contact [37] ~~The wear rate can be calculated from the following equation:~~

~~$$W = V/L\ F \quad (1)$$~~

~~where W corresponds to specific wear rates (mm^3/Nm), V is the wear volume (mm^3), L is the sliding distance (m) and F is the applied load (N). The sliding distance and applied load (i.e., 5, 10 and 15 N) for all the tested samples is the same. Therefore the only difference in wear rate is due to the differences in wear volume. For $Fe_{0.5}$, the shallow grooves indicate the lowest wear volume and therefore lowest wear rate, which agrees with the lowest mass loss values (Fig. 5).~~

These results cannot be compared with the literature since, to the authors knowledge, this is the first attempt to link wear volume to surface roughness. However, a clear trend is observed and the results are consistent with those obtained from our other experiments. It is important to point out that the wear mechanism is the same (i.e., combination of abrasion, adhesion and delamination) for all the compositions. If the wear mechanism for the tested samples was different, it might not be possible to

correlate the wear volume and surface roughness ~~might not be possible~~ and this is something we aim to study in the future.

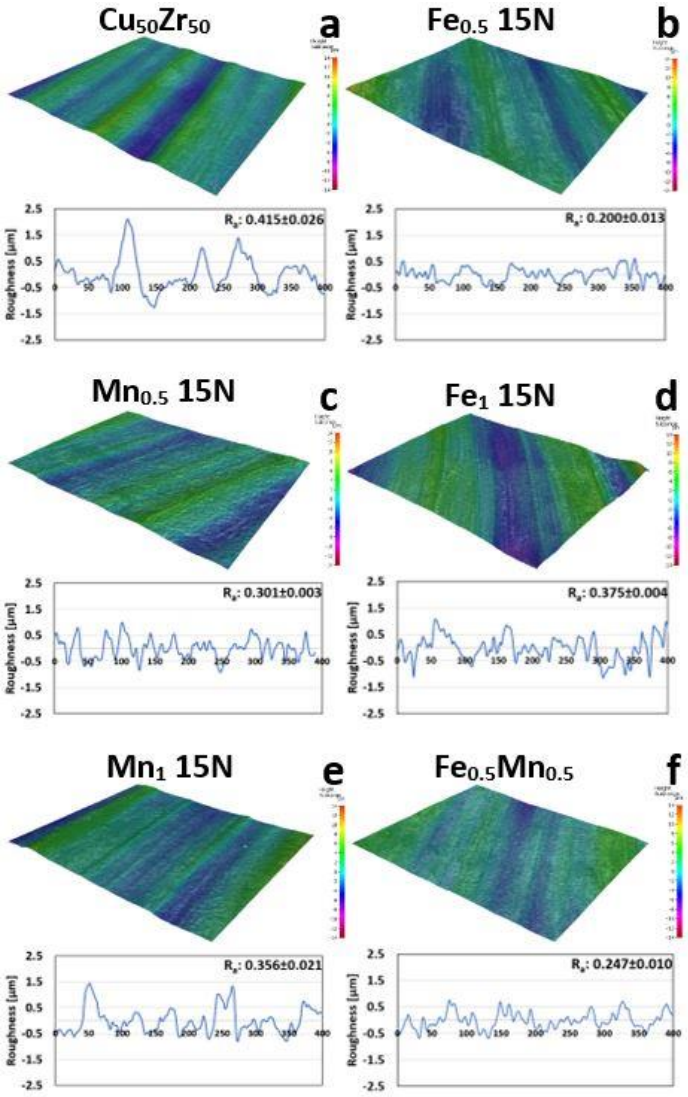

Fig. ~~9~~10. Surface topography for the different compositions after wear tests at 15 N load for 1 hour.

3.5. Structural characterization after wear tests

To better understand the microstructural changes that take place in the alloys during the wear tests after 1 hour and 15 N load, XRD scans have been done before and after the wear tests.

Fig. 11 shows the XRD patterns for $Cu_{50}Zr_{50}$, $Cu_{49.5}Zr_{50}Fe_{0.5}$, $Cu_{49}Zr_{50}Fe_{1}$, $Cu_{49.5}Zr_{50}Mn_{0.5}$, $Cu_{49}Zr_{50}Mn_{1}$ and $Cu_{49}Zr_{50}Fe_{0.5}Mn_{0.5}$ at. % alloys in the as-cast condition (i.e., AC) and the after the wear tests (i.e., AT). The XRD scans for the six compositions show peaks at similar angles associated to the following phases:

austenite B2 CuZr (a= 3.2562 nm, b = 3.2562 nm, c = 3.2562 nm), monoclinic martensite B19′ CuZr (a = 0.3237 nm, b = 0.4138 nm, c= 0.5449 nm), orthorhombic $Cu_{10}Zr_7$ (a = 0.9347 nm, b = 0.9347 nm, c = 1.2675 nm), orthorhombic Cu_8Zr_3 (a = 0.78686 nm, b = 0.81467 nm, c = 0.9977 nm) and tetragonal $CuZr_2$ (a = 0.3220 nm, b = 0.3220 nm, c= 1.1183 nm). The intensity of the peaks associated to austenite decreases after the wear tests while the intensity of the peaks corresponding to martensite increase. This indicates that a martensitic transformation has taken place during the wear tests. For all as-cast and tested samples, peaks associated with B2 CuZr austenite are detected at around 39.4º and 70.8°. In addition, martensite peaks at around 27.4°, 35.9º, 43.7° and 56.5º are detected along with peaks associated to the intermetallic phases $CuZr_2$, Cu_8Zr_3 and $Cu_{10}Zr_7$.

The wear tested $Cu_{50}Zr_{50}$ alloy (Fig. 11a) shows a slight decrease in intensity of XRD peaks at 39.4º and 71.1º associated to austenite, while the peak at 35.9° associated to martensite increases in magnitude compared to the as cast (non tested) alloy. This suggests that austenite has partly transformed into martensite. The intensity of XRD peaks of austenite for $Cu_{50}Zr_{50}$ decreased by about 28% after testing while for martensite the intensity increased by about 10%. Peaks associated to other intermetallics such as $CuZr_2$, Cu_8Zr_3 and $Cu_{10}Zr_7$ have also been detected. Microalloying with $Fe_{0.5}$ (Fig. 11b) results in large decrease in intensity of the austenite peak (58% decrement after test) and a large intensity increase of martensite peak (50% increase after test). These changes are clearly more noticeable than for $Cu_{50}Zr_{50}$ (Fig. 11a) and Fe_1 (Fig. 11c) alloys and the effect of microalloying with Fe_1 seems to have an intermediate effect between the base alloy and $Fe_{0.5}$.

These results suggest that the stress-induced martensitic transformation is most effective for the $Fe_{0.5}$ alloy and it is consistent not only with the SFE (Fig. 2), 0.26 J/m^2, but also with the mass loss (Fig. 5a), 0.0123 g at 15 N load, both of which are the smallest among all the compositions. Although for $Mn_{0.5}$ alloy (Fig. 11d) the intensity of austenite decreased by 62% after the wear test, the intensity of the peaks associated to martensite do not seem to increase, especially when compared to the alloy with $Fe_{0.5}$. However, from the relative intensity of XRD peaks it can be deduced that the volume fraction of intermetallic phases ($CuZr_2$ and $Cu_{10}Zr_7$) increased by about 10% after testing. Considering that these intermetallics are hard, they could have also contributed towards the higher wear resistance. This is consistent with the higher SFE (Fig. 2) for $Mn_{0.5}$ (0.27 J/m^2) compared to that for $Fe_{0.5}$ (0.26 J/m^2) and

therefore the lower ability for the Mn-containing alloy to transform into martensite. In fact, the mass loss (Fig. 5a) of $Mn_{0.5}$ (0.014 g) is slightly higher than that of Fe0.5 (0.0123 g). The microstructural changes for $Mn_{0.5}$ are very similar to those observed in the $Fe_{0.5}Mn_{0.5}$ alloy (Fig. 11f) as can be deduced from the similar XRD scans before and after the wear tests. For the alloy containing Mn_1 (Fig. 11e) after the wear test, the peak associated to austenite at about 39.4º, decreases in intensity by about 60%, while for martensite it increases after the test by 26%. The peaks associated to martensite overlap with broad peaks associated to different phases. The formation of these peaks may suggest that dynamic recrystallization has taken place, something that was previously observed for wear tested copper [38].

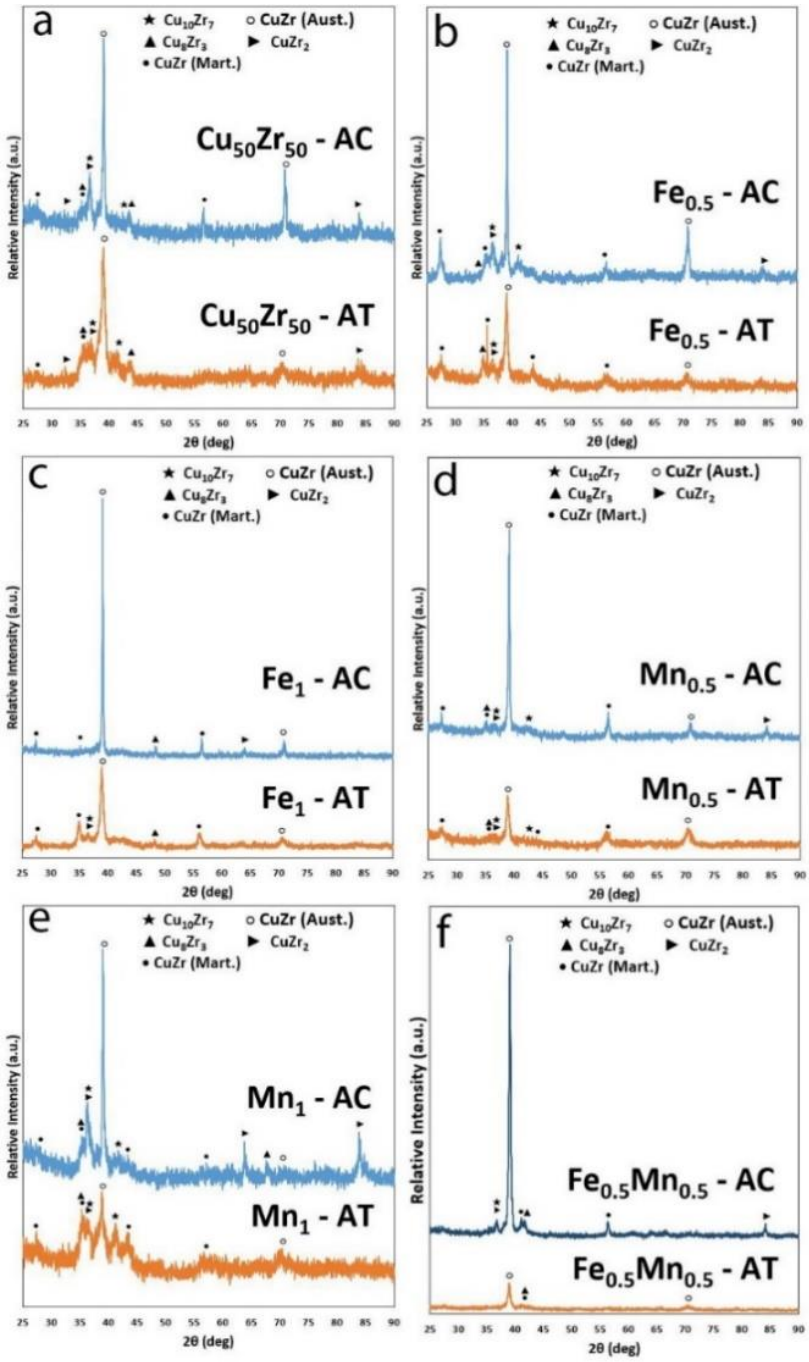

Fig. ~~10~~11. XRD scan of 2 mm diameter as-cast (AC) and after wear tested (AT) alloys with 15 N load for (a) $Cu_{50}Zr_{50}$, (b) $Cu_{49.5}Zr_{50}Fe_{0.5}$, (c) $Cu_{49}Zr_{50}Fe_1$, (d) $Cu_{49.5}Zr_{50}Mn_{0.5}$ and (e) $Cu_{49}Zr_{50}Mn_1$ and (f) $Cu_{49}Zr_{50}Fe_{0.5}Mn_{0.5}$.

To understand the effect of the microalloying elements on the wear behaviour of CuZr-based SMAs, TEM analysis has been performed. The nominal composition of as-cast $Cu_{50}Zr_{50}$ was studied by TEM in order to have a reference parent sample (i.e., without microalloying or load applied). The results from TEM have been compared with those from XRD since the former gives local information while the latter provides average

information from the microstructure. The XRD scan of Fig. 11a for as-cast $Cu_{50}Zr_{50}$ indicates the presence of multiple intermetallic phases whose peaks overlap at certain angles, for example, at 37.2º peaks associated to $Cu_{10}Zr_7$ and $CuZr_2$ are detected. To corroborate the presence of intermetallic phases, the microstructure has been studied by TEM. A bright field TEM image (Fig. 12a) of a representative microstructure of the as-cast $Cu_{50}Zr_{50}$ sample is shown. The arrow in the TEM image of Fig. 12a points towards a crystalline phase from where a Selected Area Electron Diffraction Pattern (SAED) pattern was taken (image on the right of Fig. 12a). The crystalline phase has a concentration in Cu of (53.56 at. %) and Zr of (46.44 at. %) according to EDX and thus would correspond to $Cu_{10}Zr_7$. The SAED pattern taken along the zone axis [00-1] confirms the formation of a crystalline phase with orthorhombic structure $Cu_{10}Zr_7$.

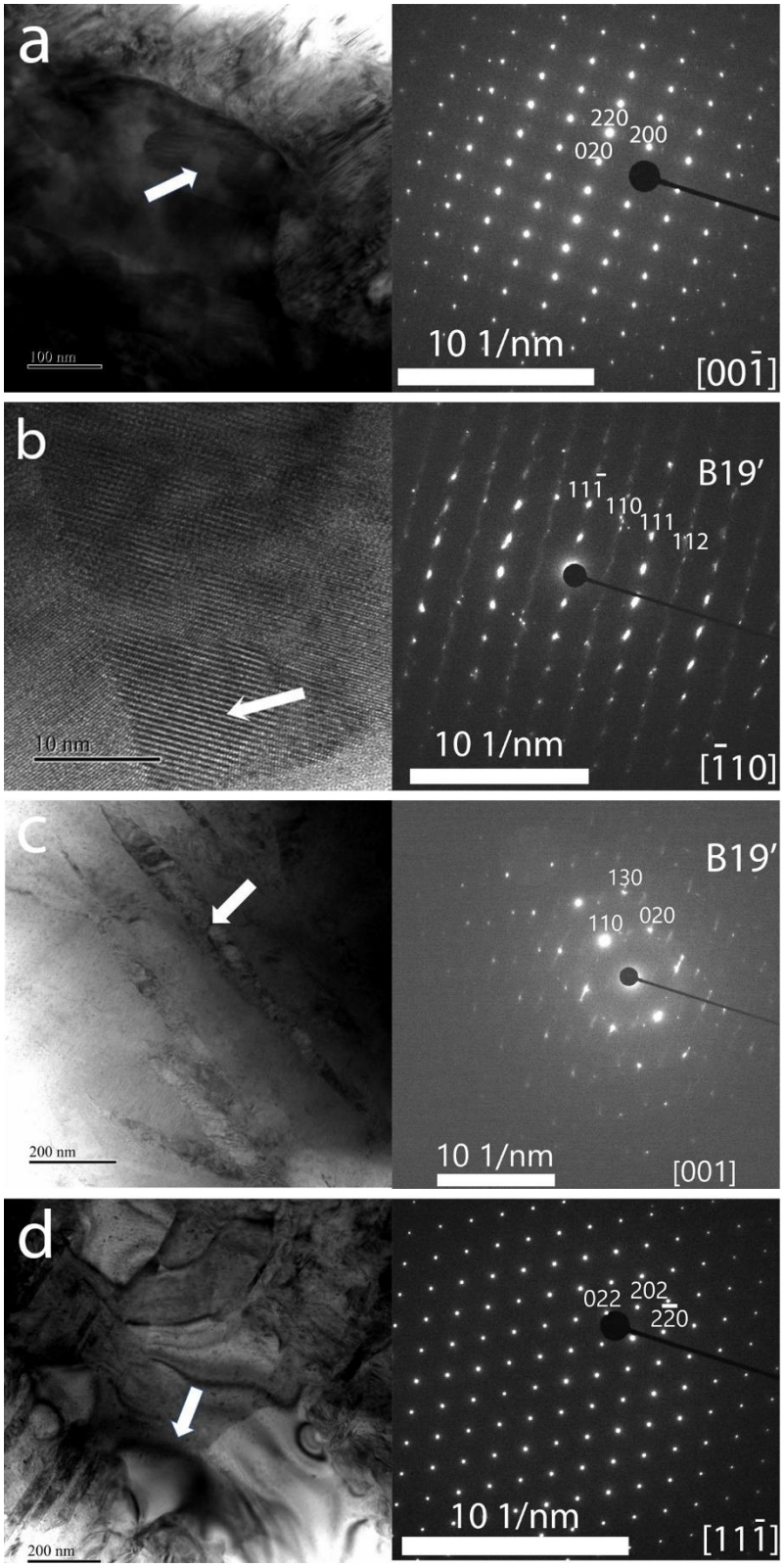

Fig. ~~11~~12. Bright field TEM images after wear tests at 15 N load and corresponding SAED pattern with zone axis B for (a) as-cast $Cu_{50}Zr_{50}$ alloy (B = [00-1]), (b) $Cu_{49.5}Zr_{50}Fe_{0.5}$ alloy (B = [-110]) and spots for B19' martensite twinned phase, (c) $Cu_{49}Zr_{50}Mn_{0.5}$ alloy (B = [001]) and spots for the B19' martensite twinned phase and (d) $Cu_{49}Zr_{50}Mn_1$ alloy (B = [11-1]).

As previously commented in section 3.4, the $Cu_{49.5}Zr_{50}Fe_{0.5}$ alloy exhibited the highest relative wear resistance (Fig. 5), especially at 15 N load, which was attributed to deformation twinning [3]. To investigate this in detail, the $Cu_{49.5}Zr_{50}Fe_{0.5}$ sample wear tested at 15 N load has been analysed by TEM. The bright field TEM image of a twinned structure (see arrow) of the $Cu_{49.5}Zr_{50}Fe_{0.5}$ sample wear tested with 15 N load is shown in Fig. 12b along with the corresponding SAED pattern taken along zone axis [-110]. This pattern indicates that the twinned structure corresponds to the monoclinic structure (P21/m, space group 11) of B19' CuZr (i.e., martensite). The presence of martensite in this Fe-containing alloy suggests that the martensitic transformation is promoted, and this agrees with our first principles simulations (see Fig. 2) and the XRD scans (Fig. 11b) since the peak intensity ratio of martensite to austenite increases after the wear tests. EDX analysis indicated that the composition of this phase is Cu (52.18 at. %), Zr (46.92 at. %) and Fe (0.9 at. %) and thus it would correspond to CuZr with Fe present in solid solution. Although the concentration of Fe in solid solution seems to be slightly higher than that of the nominal composition, one has to take into consideration that TEM is a very local technique. This means that the concentration of Fe might not be the same across all the grains but the average value is close to the nominal composition as detected by SEM-EDX (Fig. 3).

Fig. 12c shows a bright field TEM image of $Cu_{49.5}Zr_{50}Mn_{0.5}$ at. % alloy tested at 15 N. The corresponding SAED pattern indexed along the [001] zone axis also shows the presence of a monoclinic structure (P21/m, space group 11) corresponding to B19' CuZr. The detection of martensite suggests that the addition of 0.5 at. % Mn also promotes the martensitic transformation but less efficiently than for 0.5 at. % Fe as the first principles simulations in Fig. 2 suggest. These results are also in agreement with the XRD results of Fig. 11d as the intensity of the austenite peak significantly decreased after testing and volume fraction of martensite increased. The phase composition is Cu (39.32 at. %), Zr (60.04 at. %) and Mn (0.64 at. %) and thus it would correspond to CuZr with Mn in solid solution. To investigate in detail the microstructure of the as-cast $Cu_{49}Zr_{50}Mn_1$ at. % alloy, whose overall microstructure was studied before (Fig. 3f), TEM study is done. Bright field TEM image of Fig. 12d shows the microstructure consisting of small phases of up to 200 nm long. For one of the crystalline phases (see arrow in Fig. 12d) a SAED pattern was obtained from the zone axis [11-1] and this pattern would correspond to an orthorhombic structure $Cu_{10}Zr_7$ (Aba2, space group 41). This crystalline phase has a chemical composition of

$Cu_{61.34}Zr_{38.66}$ at. % and therefore, from the ratio of the elements, this phase would correspond to the intermetallic $Cu_{10}Zr_7$ phase.

4. Conclusions

The following conclusions can be drawn:

-Changes in the Stacking Fault Energy of B2 CuZr austenite upon partial replacement of Cu by a microalloying element has been analysed from first principles calculations to predict the ability of austenite to transform into martensite upon wear testing. This has been done in the present work to select the microalloying elements (Fe and Mn) and their concentrations (0.5 and 1 at. %) for maximum wear resistance,

-For pin-on-disc wear tests at 10 N load, the mass loss values are similar for all compositions, ranging from 0.00875 to 0.011 g, and become more similar, values around 0.00255 g, as the load decreases to 5 N. This indicates that the stress-induced martensitic transformation upon twinning becomes less relevant as the load decreases.

-For 15 N load wear tests, differences in mass loss are larger than for 5 and 10 N, ranging from a minimum of 0.0123 g for 0.5 at. % Fe to a maximum of 0.0177 g for $Cu_{50}Zr_{50}$ alloy. The lowest wear volume and therefore lowest specific wear rate, around 5.9 mm^3/Nm is attained by 0.5 at. % Fe, compared to 8.5 for mm^3/Nm for $Cu_{50}Zr_{50}$ at 15 N load, which agrees with the lowest mass loss value. The low mass loss and specific wear rate values are attributed to the promotion of the transformation from austenite into the harder and therefore more wear resistant stress-induced B19' martensite as proven from TEM and XRD results. The more wear resistant samples exhibit not only lower friction coefficient but also more shallow abrasive groves, indicating the lowest wear volume and lowest wear rate.

- From the cross section of the pins after sliding wear tests, wear mechanisms of abrasion, adhesion and delamination have been identified. This can be deduced from the presence of long continuous grooves, the removal of material onto the disc and presence of subsurface cracks respectively.

-For 15 N load, partial replacement of Cu from the $Cu_{50}Zr_{50}$ shape memory alloy (SMA) by 0.5 at. % Fe, results in a lifetime enhancement of the $Cu_{50}Zr_{50}$ alloy of about 30.5 % while for 0.5 at. % Mn the lifetime enhancement is about 21 %. Microalloying is

therefore an efficient strategy to develop Cu-Zr-based shape memory alloys as temperature adaptive shaft seals for engines. The shaft is generally made out of stainless steel and the contact surface and force between the shaft and the seal are of the same order of magnitude as those investigated in this manuscript. The ability to enhance the wear resistance of $Cu_{50}Zr_{50}$ austenite via optimum microalloying is promising to develop wear resistant shaft seals with enhanced lifetime.

Acknowledgments

This work has been partially financed by EPSRC (EP/P019889/1) First Grant scheme. S.G. acknowledges this research contract from EPSRC. A. Younes acknowledges research support from Northumbria University. We acknowledge Durham HPC facility Hamilton and the national HPC facility Archer for compute resources. We wish to acknowledge the support of the Henry Royce Institute for A. Younes through the Royce PhD Equipment Access Scheme enabling access to TEM facilities at Henry Royce Institute, University of Sheffield; EPSRC Grant Number EP/R00661X/1.

References

1. Mohd Jani, J., et al., *A review of shape memory alloy research, applications and opportunities.* Materials & Design (1980-2015), 2014. **56**: p. 1078-1113.
2. Ma, J., I. Karaman, and R.D. Noebe, *High temperature shape memory alloys.* International Materials Reviews, 2010. **55**(5): p. 257-315.
3. Younes, A., et al., *Wear rate at RT and 100 °C and operating temperature range of microalloyed Cu50Zr50 shape memory alloy.* Journal of Alloys and Compounds, 2020. **817**: p. 153330.
4. Jackson, C., H. Wagner, and R. Wasilewski, *55-Nitinol-The Alloy with a Memory: It's Physical Metallurgy Properties, and Applications. NASA SP-5110.* NASA Special Publication, 1972. **5110**.
5. Nnamchi, P., A. Younes, and S. González, *A review on shape memory metallic alloys and their critical stress for twinning.* Intermetallics, 2019. **105**: p. 61-78.
6. Tan, L. and W.C. Crone, *In situ TEM observation of two-step martensitic transformation in aged NiTi shape memory alloy.* Scripta Materialia, 2004. **50**(6): p. 819-823.
7. Xie, J.-X., J.-L. Liu, and H.-Y. Huang, *Structure design of high-performance Cu-based shape memory alloys.* Rare Metals, 2015. **34**(9): p. 607-624.
8. De Luca, F., et al., *Stress-induced martensitic transformation of Cu50Zr50 shape memory alloy optimized through microalloying and co-microalloying.* Journal of Alloys and Compounds, 2019. **781**: p. 337-343.
9. Wu, Y., et al., *Ductilizing Bulk Metallic Glass Composite by Tailoring Stacking Fault Energy.* Physical Review Letters, 2012. **109**(24): p. 245506-1-245506-12.
10. Hattori, S. and A. Tainaka, *Cavitation erosion of Ti–Ni base shape memory alloys.* Wear, 2007. **262**(1): p. 191-197.
11. González, S., et al., *Drastic influence of minor Fe or Co additions on the glass forming ability, martensitic transformations and mechanical properties of shape memory Zr–Cu–Al bulk*

metallic glass composites. Science and Technology of Advanced Materials, 2014. **15**(3): p. 035015.
12. González, S., *Role of minor additions on metallic glasses and composites.* Journal of Materials Research, 2016. **31**(1): p. 76-87.
13. Segall, M.D., et al., *First-principles simulation: ideas, illustrations and the CASTEP code.* Journal of Physics: Condensed Matter, 2002. **14**(11): p. 2717-2744.
14. Clark, S.J., et al., *First principles methods using CASTEP.* Zeitschrift für Kristallographie-Crystalline Materials, 2005. **220**(5/6): p. 567-570.
15. De Cooman, B.C., et al. *State-of-the-Science of High Manganese TWIP Steels for Automotive Applications*. 2009. London: Springer London.
16. Duerig, T., K. Melton, and J. Proft, *Wide hysteresis shape memory alloys.* Engineering aspects of shape memory alloys, 1990. **130**.
17. Tadaki, T., *Shape memory materials*. Shape Memory Materials, ed. K. Otsuka and C.M. Wayman. 1998, Cambridge; New York: Cambridge University Press.
18. Gustmann, T., et al., *Properties of Cu-Based Shape-Memory Alloys Prepared by Selective Laser Melting.* Shape Memory and Superelasticity, 2017. **3**(1): p. 24-36.
19. Wang, D., et al., *Bulk metallic glass formation in the binary Cu–Zr system.* Applied Physics Letters, 2004. **84**(20): p. 4029-4031.
20. Villapún, V.M., et al., *Tuning the Mechanical and Antimicrobial Performance of a Cu-Based Metallic Glass Composite through Cooling Rate Control and Annealing.* Materials, 2017. **10**(5): p. 506.
21. Lejaeghere, K., et al., *Reproducibility in density functional theory calculations of solids.* Science, 2016. **351**(6280): p. aad3000.
22. Perdew, J., K. Burke, and M. Ernzerhof, *Generalized Gradient Approximation Made Simple: Physical Review Letter*. 1996, ISSN.
23. Foreman, J., S. Sauerbrunn, and C. Marcozzi, *Exploring the sensitivity of thermal analysis techniques to the glass transition.* TA Instruments: Applications Library Search [online], 2006.
24. Fabregat-Sanjuan, A., et al., *Identifying the effects of heat treatment temperatures on the Ti50Ni45Cu5 alloy using dynamic mechanical analysis combined with microstructural analysis.* Materials Science and Engineering: A, 2018. **712**: p. 281-291.
25. Archard, J., *Contact and rubbing of flat surfaces*. Journal of applied physics, 1953. **24**(8): p. 981-988.
26. Pan, X.F., et al., *Vickers hardness and compressive properties of bulk metallic glasses and nanostructure-dendrite composites*. Journal of materials research, 2005. **20**(10): p. 2632-2638
27. Rahaman, M.L., Zhang, L., Liu, M. and Liu, W., *Surface roughness effect on the friction and wear of bulk metallic glasses*. Wear, 2015. 332, p. 1231-1237.
28. Liu, Y., Yitian, Z., Xuekun, L. and Liu, Z., Wear behavior of a Zr-based bulk metallic glass and its composites. Journal of alloys and compounds, 2010. **503**(1), p. 138-144.
29. Suh, N. P. Tribophysics. Englewood Cliffs, N.J., Prentice-Hall, 1986.
30. Zum Gahr, K.H., *Microstructure and wear of materials*. Vol. 10. 1987.
31. Li, Y.C., Zhang, C., Xing, W., Guo, S.F. and Liu, L., *Design of Fe-based bulk metallic glasses with improved wear resistance*. ACS applied materials & interfaces, 2018. **10**(49), p. 43144-43155.
32. Madhu, H.C., Edachery, V., Lijesh, K.P., Perugu, C.S. and Kailas, S.V., *Fabrication of Wear-Resistant Ti 3 AlC 2/Al 3 Ti Hybrid Aluminum Composites by Friction Stir Processing*. Metallurgical and Materials Transactions A, 2020. 51, p. 4086-4099.
33. Huang, Y., Fan, H., Wang, D., Sun, Y., Liu, F., Shen, J., Sun, J. and Mi, J. *The effect of cooling rate on the wear performance of a ZrCuAlAg bulk metallic glass*. Materials & Design, 2014. 58, p. 284-289.
34. Blau, P.J. and Komanduri, R., *Friction and Wear Transitions of Materials: Break-in, Run-in, and Wear-in*., 1990

35. Villapún, V.M., Medina, J., Pérez, P., Esat, F., Inam, F. and González, S., *Strategy for preventing excessive wear rate at high loads in bulk metallic glass composites*. Materials & Design, 2017, 135, p. 300-308.
36. Bhatt, J., Kumar, S., Dong, C. and Murty, B.S., *Tribological behaviour of Cu60Zr30Ti10 bulk metallic glass*. Materials Science and Engineering: A, 2007. **458**(1-2), p. 290-294.
37. Modern Tribology Handbook: Volume One: Principles of Tribology1, Koji Kato, K. Adachi. Wear mechanisms, 2000, p. 273-300.
38. Yao, B., Z. Han, and K. Lu, *Correlation between wear resistance and subsurface recrystallization structure in copper.* Wear, 2012. **294-295**: p. 438-445.